Divergence Prior and Vessel-tree Reconstruction

Zhongwen Zhang[1] Dmitrii Marin[1] Egor Chesakov[2]
Marc Moreno Maza[2] Maria Drangova[3] Yuri Boykov[1]

[1] University of Waterloo, Canada [2] Western University, Canada [3] Robarts Research, Canada

Abstract

We propose a new geometric regularization principle for reconstructing vector fields based on prior knowledge about their divergence. As one important example of this general idea, we focus on vector fields modelling blood flow pattern that should be divergent in arteries and convergent in veins. We show that this previously ignored regularization constraint can significantly improve the quality of vessel tree reconstruction particularly around bifurcations where non-zero divergence is concentrated. Our divergence prior is critical for resolving (binary) sign ambiguity in flow orientations produced by standard vessel filters, e.g. *Frangi. Our vessel tree centerline reconstruction combines divergence constraints with robust curvature regularization. Our unsupervised method can reconstruct complete vessel trees with near-capillary details on synthetic and real 3D volumes.*

1. Background on vessel detection

There is a large body of prior work on estimation of vessels in computer vision and biomedical imaging communities [19]. Typically, pixel-level detection of tubular structures is based on multiscale eigen analysis of raw intensity Hessians developed by Frangi et al. [11] and other research groups [10]. At any given point (pixel/voxel) such vessel enhancement filters output a *tubularness measure* and estimates of the vessel's scale and orientation, which describes the flow direction upto to a sign. While such local analysis of Hessians is very useful, simple thresholding of points with large-enough vesselness measure is often unreliable as a method for computing the vessel tree structure. While thresholding works well for detecting relatively large vessels, detection of smaller vessels is complicated by noise, partial voluming, and outliers (e.g. ring artifacts). More importantly, standard tubular filters exhibit signal loss at vessel bifurcations as those do not look like tubes.

Earlier regularization methods [30, 31] address many tree reconstruction challenges due to noise and outliers assuming accurately localized "anchor" points are available and data is relatively small. In contrast, we focus on large 3D data with 80% of near-capillary vessels of voxel-size or less; thus, finding accurate centerline anchors is problematic due to signal loss at thinner parts and bifurcations. We propose a new regularization prior based on knowledge of the flow pattern divergence. It is critical for disambiguating flow directions and gives important cues on the vessel tree structure. Next subsections outline related regularization methods for vessel reconstruction and motivate our work.

It may be also interesting to apply deep learning to vessel tree detection, but neural network training is problematic since vessel tree ground truth is practically impossible in real 3D data. Practical weakly-supervised training may require regularized loss functions [29] appropriate for vessel tree detection. While our regularization methodology may help to design such losses, we leave this for future work.

1.1. Vessel representation: centerline or segment

Two common approaches to representing vessels in reconstruction methods are volumetric binary mask and centerline. Volumetric mask is typical for techniques directly computing vessel segmentation, *i.e*. binary labeling of pixels/voxels. In contrast, centerline is a 1D abstraction of the vessel. But, if combined with information about vessel radii, it is easy to obtain a volumetric mask or segmentation from the vessel's centerline, e.g. using MAT [27]. Vice versa, centerline could be estimated from the vessel's binary mask using skeletonization algorithms.

In the context of regularization methods for vessel reconstruction, centerline representation offers significant advantages since powerful higher-order regularizers are easier to apply to 1D structures. For example, centerline's curvature can be regularized [18], while conceptually comparable regularization for vessel segmentation requires optimization of Gaussian or minimum curvature of the vessel's surface with no known practical algorithms. In general, curvature remains a challenging regularization criteria for surfaces [25, 28, 14, 24, 21]. Alternatively, some vessel segmentation methods use simpler first-order regularizers producing minimal surfaces. While tractable, such regularizers impose a wrong prior for surfaces of thin structures due to their bias to compact blob shapes (a.k.a. shrinking bias).

1.2. Towards whole tree centerline

Many vessel reconstruction methods directly compute centerlines of different types that can be informaly defined as simplified (e.g. regularized) 1D representation of the blood flow *pathlines*. For example, the A/B shortest path methods require a user to specify two end points of a vessel and apply Dijkstra to find an optimal pathline on a graph with edge weights based on vesselness measure.

Interactive A/B methods are not practical for large vessel tree reconstraction problems. While it is OK to ask a user to identify the tree *root*, manual identification of all the end points (*leaves*) is infeasible. There are *tracing* techniques [3] designed to trace vessel tree from a given root based on vesselness measures and some local continuation heuristics. Our evaluations on synthetic data with groud truth show that local tracing methods do not work well for large trees with many thin vessels even if we use the ground truth to provide all tree leaves as extra seeds in addition to the root.

Our goal is unsupervised reconstruction of the whole vessel tree centerline. This problem can be solved in two steps: (1) compute a "tubular graph" of plausible vessel links between some centerline anchor points and (2) estimate its optimal sub-tree under given regularity constraints. It is common to do step one via simple heuristics and to focus on the optimization problems in the second step [30, 31]. In contrast, we focus on accurate estimation of the centerline points (anchors) and their connectivity graph. We use basic MST for step two, in part due to large size of our problem where ILP [30] or genetic methods [31] do not easily apply. To estimate centerline points, we optimize a global objective function for a field of centerline tangents. Such objectives can combine vesselness measures, geometric errors, and different regularization constraints addressing centerline completion. Related prior work using centerline curvature regularization is reviewed below.

1.3. Curvature regularization for centerline

Curvature, a second-order smoothness term, is a natural regularizer for thin structures. In general, curvature has been studied for image segmentation [25, 28, 26, 5, 14, 24, 21, 18], for stereo or multi-view-reconstruction [17, 23, 33], connectivity measures in analysis of diffusion MRI [20], for tubular structures extraction [18], for *inpainting* [2, 6] and edge completion [12, 32, 1].

Olsson et al. [22] propose curvature approximation for surface fitting regularization. Their framework employs tangential approximation of surfaces. The authors assume that the data points are noisy readings of the surface. The method estimates local surface patches, which are parameterized by tangent planes. The (shortest) interval from the data point to its tangent plane gives the surface normal and defines the point of tangency.

Assume there is a smooth curve, see Fig. 1. Points p and q on the curve and tangents l_p and l_q at these points are given. Then the integrals of curvature $\kappa(\cdot)$ is estimated by

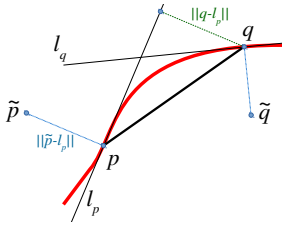

Figure 1. Curvature model of [22]. Given two points p and q on the red curve and two tangents l_p and l_q at these points, the integrals of curvature are approximated by (1–3).

$$\int_p^q |\kappa(s)| ds \approx \frac{\|p - l_q\|}{\|p - q\|}, \tag{1}$$

$$\int_p^q |\kappa(s)|^2 ds \approx \frac{\|p - l_q\|^2}{\|p - q\|^3}. \tag{2}$$

where $\|p - l_q\|$ is the distance between point p and the tangent line at point q represented by vector l_q. Olsson et al. [22] explore several similar approximations and argue that

$$\kappa_{pq}(l_p, l_q) := \frac{1}{2} \frac{\|p - l_q\|^2 + \|q - l_q\|^2}{\|p - q\|^2} \tag{3}$$

gives practically better curvature regularization[1].

Marin et al. [18] generalized this surface fitting problems to detection problems where majority of the data points, *e.g.* image pixels, do not belong to a thin structure. In order to do that they introduced binary variables in their energy indicating if a data point belongs to the thin structure. One of their applications is vessel detection. The proposed vessel-tree extraction system includes vessel enhancment filtering, non-maximum suppresion for data reduction, tangent approximation of vessels' centerline and minimum spanning tree for topology extraction. Assuming that detection variables are computed, the tangent approximation of vessels' centerline is found by minimizing energy

$$E_u(l) = \sum_p \|\tilde{p} - l_p\|^2 + \gamma \sum_{(p,q)\in N} \kappa_{pq}(l_p, l_q) \tag{4}$$

where summations are over detected vessel points, $\tilde{p}$ is the original data point's location, l_p is the tangent vector at point p, the denoised point location p is constraint to be the closest point on tangent line at p, and $N \subset \Omega^2$ is the neighborhood system. The curvature term in the energy makes the tangents "collapse" onto a one-dimensional centerline, see Fig.3(a,c). But the same figures also show artifacts around bifurcations where undesired triangular structures form, indicating unoriented tangent model limitations.

Our experiments employs the same components as in [18]. Our work focuses on analysis of failure cases and improvement of the regularization stage for tangent approximation. In particular we will show the drawbacks of curvature models (1-3) in the context of vessel tree extraction and propose a solution leading to significant improvements.

[1] Equation (3) is a symmetric form of regularizer recommended in [22].

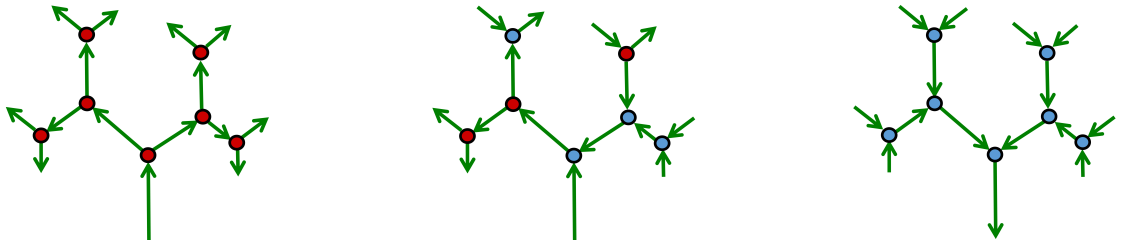

(a) divergent vessels (**arteries**) (b) inconsistent divergence (c) convergent vessels (**veins**)

Figure 2. **[Vessel-tree divergence]** Vessels are the blood flow *pathlines* and could be assigned orientations (7). To estimate orientations, we penalize negative (or positive) "vessel divergence", which we define as the divergence of oriented unit tangents of vessels/pathlines. Such *unit tangent flow* divergence is positive (red) or negative (blue) at bifurcations, see (a-c). Note that standard curvature [22, 18] and oriented curvature models (6) either can not distinguish (b) from (a) and (c) or may even prefer (b) depending on specific combinations of bifurcation angles. For example, compare vessel direction disambiguation based on curvature and the divergence prior in Fig.7 (a) & (b).

1.4. Our contributions and motivation

This work addresses an important limitation of vessel tree reconstruction methods due to sign ambiguity in vessel orientation produced by local vesselness filters, e.g. Frangi. This orientation is described by the smallest eigenvector of the local intensity Hessian, but its sign is ambiguous. Thus, the actual flow directions are not known, even though they are an important reconstruction cue particularly at bifurcations. This binary direction ambiguity can be resolved only by looking at the global configuration of vessel orientations (tangents) allowing to determine a consistent flow pattern.

We propose a divergence prior for disambiguating the global flow pattern on the vessel tree, see Fig.2. This prior can be imposed as a regularization constraint for a vector field of oriented unit tangents for vessel pathlines. We penalize negative (or positive) divergence for such unit *tangent flow* to enforce a consistent flow pattern[2]. The summary of our contributions:

- Prior knowledge about divergence is generally useful for vector field inference. We propose a way to evaluate divergence for sparsely sampled vector fields via pairwise potentials. This makes divergence constraints amenable to a wide range of optimization methods for disrcrete or continuous hidden variables.

- As an important application, we show that known divergence can disambiguate vessel directions output by standard vessel filters, *e.g*. Frangi [11]. This requires estimation of binary "sign" variables. The constraint penalizing positive (or negative) divergence is non-submodular, but it is well optimized by TRWS [15].

- To estimate vessel tree centerline, the divergence constraint can be combined with robust *oriented* curvature regularization for pathline tangents. Additional options include outlier/detection variables [18] and/or tree structure completion techniques, *e.g*. using MST.

- We provide extensive quantitative validation on synthetic vessel data, as well as qualitative results on real high-resolution volumes.

[2]This divergence constraint is specific to unit tangent flow. Note that divergence for consistent blood flow velocities is zero even at bifurcations assuming *incompressible* blood.

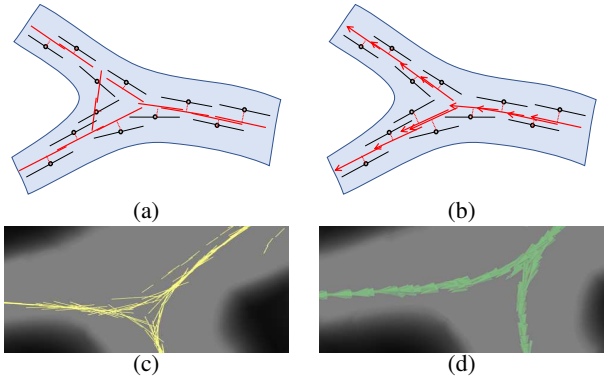

(a) (b) (c) (d)

Figure 3. Triangle artifacts at bifurcation. Optimization of energy (4) ignoring tangent orintations often leads to a strong local minima as in (a) and (c). The line segments are the estimated tangents of the centerline. New curvature term (6) takes into account tangent orientations resolving the artifacts, see (b) and (d).

The paper is organized as follows. Section 2 introduces oriented vessel pathline tangents and discusses their curvature-based regularization. It is clear that orientation of the flow at the bifurcations is important, *e.g*. see Fig.3. Section 3 introduces our divergence prior and methods for enforcing it in the context of vessel tree centerline estimation. The last sections presents our experimental results.

2. Bifurcations and curvature

2.1. Oriented curvature constraint

Previous works [22, 24, 18] ignored orientations of tangent vectors $\{l_p\}_{p\in\Omega}$. Equations (1)–(4) do not depend on the orientations of l. In practice, the orientations of vec-

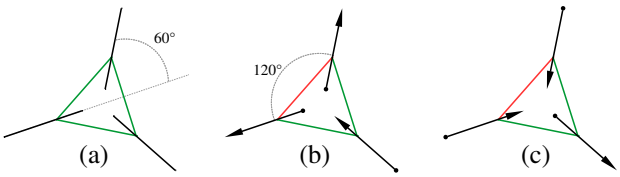

Figure 4. Illustrative examples of three interacting tangents with unoriented curvature (a) as in (4) and two alternative oriented configurations (b) and (c) with oriented curvature as in (5). The green line denotes pairwise interaction with low curvature estimate. Note, unoriented curvature (1–3) always chooses the smallest angle for calculation. The red line shows "inactive" interaction where curvature estimate (6) reaches the high saturation threshold.

tors l_p are arbitrarily defined. Ignoring the orientations in energy (4) results in significant "triangle" artifacts around bifurcation, see Fig. 3(a,c). Consider an illustrative example in Fig. 4(a). Each of the three tangents interacts with the other two. The prior knowledge about blood flow pattern dictates that among those three tangents there should be one incoming and one outcoming. Introduction of orientations allows us to distinguish the incoming/outcoming tangents and subsequently inactivate one of the interactions, see Fig. 4(b), resulting in disappearance of these artifacts.

In order to introduce oriented curvature we introduce a new vector field $\bar{l}_p$, which we call *oriented*. Then, we introduce energy $E_o(\bar{l})$ by replacing curvature term in energy (4) with a new oriented curvature as follows

$$E_o(\bar{l}) = \sum_p \|\tilde{p} - \bar{l}_p\|^2 + \gamma \sum_{(p,q)\in N} \bar{\kappa}_{pq}(\bar{l}_p, \bar{l}_q) \qquad (5)$$

where

$$\bar{\kappa}_{pq}(\bar{l}_p, \bar{l}_q) \;:=\; \begin{cases} \kappa_{pq}(\bar{l}_p, \bar{l}_q), & \langle \bar{l}_p, \bar{l}_q \rangle \geq \tau, \\ 1, & \text{otherwise}, \end{cases} \qquad (6)$$

and $\langle \bar{l}_p, \bar{l}_q \rangle$ is the dot product of $\bar{l}_p$ and $\bar{l}_q$ and $\tau \geq 0$ is a positive threshold discussed in Fig. 5.

The connection between oriented field $\bar{l}$ and l is

$$\bar{l}_p = x_p \cdot l_p \qquad (7)$$

where binary variables $x_p \in \{-1, 1\}$ flip or preserve the arbitrarily defined orientations of l_p.

2.2. Curvature and orientation ambiguity

Introduction of orientated curvature resolves triangle artifacts, see Fig. 3(b,d). However, the orientations are not known in advance. For example, the Frangi filter [11] defines a tangent as a unit eigenvector of a special matrix. The unit eigenvectors are defined up to orientation, which is chosen arbitrarily. One may propose to treat energy (5) as a function of tangent orientations x via relation (7) as follows

$$E_o(x) \;:=\; E_o(\{x_p \cdot l_p\})\Big|_{l_p = const} \qquad (8)$$

Figure 5. Robustness of curvature (6). The pairs of tangent vectors that has angle greater than $\arccos\tau$ are not considered belonging to the same vessel. A constant penalty is assigned to such pairs. This "turns off" smoothness enforcement at bifurcations.

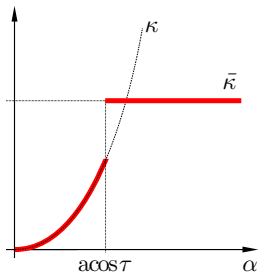

(a) Voronoi cells for $p, q \in \Omega$ and facet f_{pq}

(b) ϵ-thin box f^{ϵ}_{pq} around facet f_{pq}

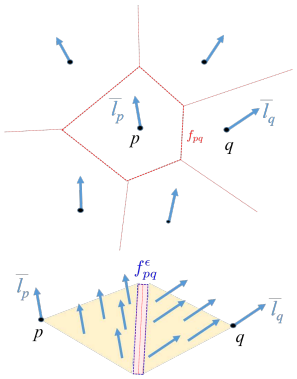

Figure 6. Divergence of a sparse vector field $\{\bar{l}_p | p \in \Omega\}$. Assuming that the corresponding "extrapolated" dense vector field is constant inside Voronoi cells (a), it is easy to estimate (non-zero) divergence $\nabla \bar{l}_{pq}$ (9) concentrated in a narrow region f^{ϵ}_{pq} around each facet (b) using the divergence theorem.

However, energy (8) is under-constrained because it allows multiple equally good solutions, see Fig. 4(b) and (c). The example in (b) shows a divergent pattern while (c) shows a convergent pattern suggesting artery/vein ambiguity. Unfortunately, energy (8) does not enforce consistent flow pattern across the vessel tree resulting in a mix of divergent and convergent bifurcations as in Fig. 2(b). Real data experiments confirm this conclusion, see Fig. 7(a).

Thus, oriented curvature model (5) has a significant problem. While it can resolve "triangle artifacts" at bifurcations, see Fig.3, it breaks the wrong sides of the triangles at many bifurcations: it estimates the flow pattern incorrectly and then give the incorrect estimation of centerline, see Fig.8(a). Below we introduce our divergence prior directly enforcing consistent flow pattern over the vessel tree.

3. Divergence constraint

3.1. Estimating divergence

Figure 6 describes our (finite element) model for estimating divergence of a sparse vector field $\{\bar{l}_p | p \in \Omega\}$ defined for a finite set of points $\Omega \subset \mathcal{R}^3$. We extrapolate the vector field over the whole domain $\mathcal{R}^3$ assuming constancy of the vectors on the interior of the Voronoi cells for $p \in \Omega$, see Fig.6(a). Thus, vectors change only in the (narrow) region around the cell facets where all non-zero divergence is con-

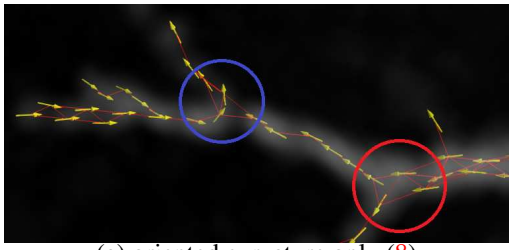

(a) oriented curvature only (8)

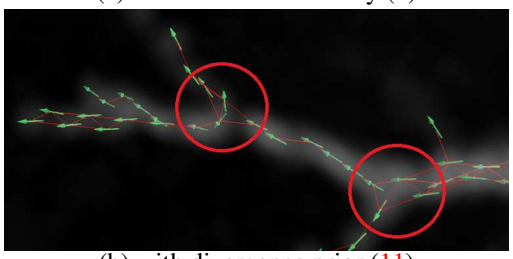

(b) with divergence prior (11)

Figure 7. Disambiguating flow directions in Frangi output [11]. Both examples use fixed (unoriented) vessel tangents $\{l_p\}$ produced by the filter and compute (oriented) vectors $\bar{l}_p = x_p l_p$ (7) by optimizing binary sign variables $\{x_p\}$ using energies (8) in (a) and (11) in (b). The circles indicate divergent (red) or convergent (blue) bifurcations similarly to the diagrams in Fig.2. The extra divergence constraint in (10) enforces flow pattern consistency (b).

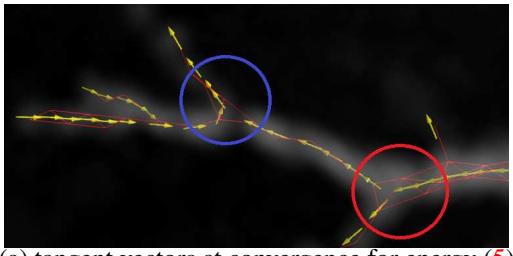

(a) tangent vectors at convergence for energy (5)

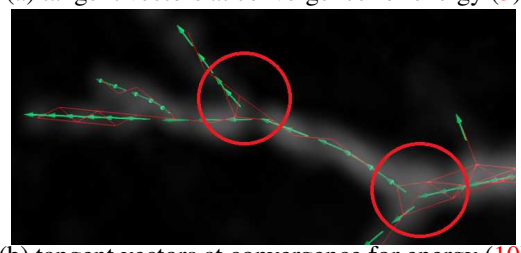

(b) tangent vectors at convergence for energy (10)

Figure 8. Centerline estimation for the data in Fig.7. Instead of showing tangent orientations estimated at the first iteration as in Fig.7, we now show the final result at convergence for minimizing energy (5) in (a) and energy (10) in (b). The blue circle shows bifurcation reconstruction artifacts due to the wrong estimation of vessel orientations in Fig.7(a).

centrated. To compute the integral of divergence in the area between two neighboring points $p, q \in \Omega$, see Fig.6(b), we estimate flux of the extrapolated vector field over ϵ-thin box f^{ϵ}_{pq} around facet f_{pq}

$$\int_{f^{\epsilon}_{pq}} \langle \bar{l}, n_s \rangle \, ds \;\; = \;\; \frac{\langle \bar{l}_q, pq \rangle - \langle \bar{l}_p, pq \rangle}{|pq|} \cdot |f_{pq}| \;\; + \;\; o(\epsilon)$$

where n_s is the outward unit normal of the box and $|f_{pq}|$ is the facet's area. Then, divergence theorem implies the following formula for the integral of divergence of the vector field inside box f^{ϵ}_{pq}

$$\nabla \bar{l}_{pq} \;\; = \;\; \frac{\langle \bar{l}_q, pq \rangle - \langle \bar{l}_p, pq \rangle}{|pq|} \cdot |f_{pq}| \qquad (9)$$

where we ignore only infinitesimally negligible $o(\epsilon)$ term.

3.2. Oriented centerline estimation

Constraints for divergence $\nabla \bar{l}_{pq}$ in the regions between neighbors $p, q \in \mathcal{D}$ in Delaugney triangulation of Ω can be combined with $E_o(\bar{l})$ in (5) to obtain the following joint energy for estimating oriented centerline tangents $\bar{l}_p$

$$E(\bar{l}) \;\; = \;\; E_o(\bar{l}) \;\; + \;\; \lambda \sum_{(p,q)\in\mathcal{D}} (\nabla \bar{l}_{pq})^{-} \qquad (10)$$

where the negative part operator $(\cdot)^{-}$ encourages divergent flow pattern as in Fig.2(a). Alternatively, one can use $(\cdot)^{+}$ to encourage a convergent flow pattern as in Fig.2(c). This joint energy for oriented centerline estimation $E(\bar{l})$ combines Frangi measurements, centerline curvature regularity, and consistency of the flow pattern, see Fig.7(b). Note that specific value of facet size in (9) had a negligible effect in our centerline estimation tests as it only changes a relative weight of the divergence penalty at any given location. For simplicity, one may use $|f_{pq}| \approx const$ for all $p, q \in \mathcal{D}$.

Optimization of oriented centerline energy $E(\bar{l})$ in (10) over oriented tangents $\{\bar{l}_p\}$ can be done via block-coordinate descent. As follows from definition (7)

$$E(\bar{l}) \;\; \equiv \;\; E(\{x_p \cdot l_p\}).$$

We iterate TRWS [15] for optimizing non-submodular energy for binary "sign" disambiguation variables $\{x_p\}$

$$E(x) \;\; := \;\; E(\{x_p \cdot l_p\})\Big|_{l_p = const} \qquad (11)$$

and *trust region* [34, 18] for optimizing robust energy for aligning tangents into 1D centerline

$$E(l) \;\; := \;\; E(\{x_p \cdot l_p\})\Big|_{x_p = const}. \qquad (12)$$

Figure 9 shows a representative example illustrating convergence of energy (10) in a few iterations.

Note that the divergence constraint in joint energy (10) resolves the problem of under-constrained objective (5) discussed at the end of Section 2. Since the flow pattern consistency is enforced, optimization of (10) should lead to a consistent resolution of the triangle artifacts at bifurcations. see Fig.8(b). Our experimental results support this claim.

Figure 9. Representative example of the decrease in energy (10) for block-coordinate descent iterating optimization of (11) and (12). For initialization, we use raw undirected tangents $\{l_p\}$ generated by Frangi filter [11]. Then, we iteratively reestimate binary sign variables $\{x_p\}$ and unoriented tangents $\{l_p\}$.

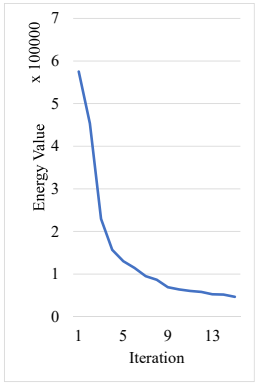

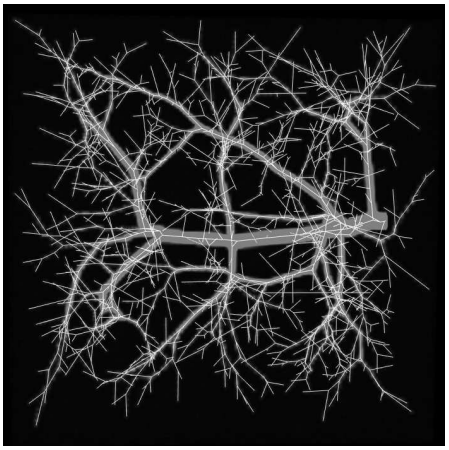

Figure 10. An example of one volume synthetic data. The white lines inside vessels denote ground truth of centerline.

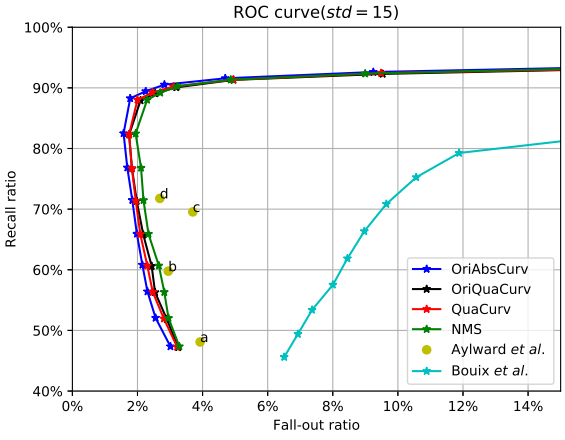

Figure 11. Detection of centerline points: comparison of our methods (OriAbsCurv and OriQuaCurv), unoriented quadratic curvature (QuaCurv) [18], non-maximum suppression (NMS), SegmentTubes (Aylward *et al.* [3]) and medial axis extraction (Bouix *et al.* [4]). The four letters on yellow dots denote different seed point lists: (a) using root and all leaf points; (b) using 50% of all bifurcations and leaf points; (c) using middle points of all branch segments; (d) using all bifurcations and leaf points.

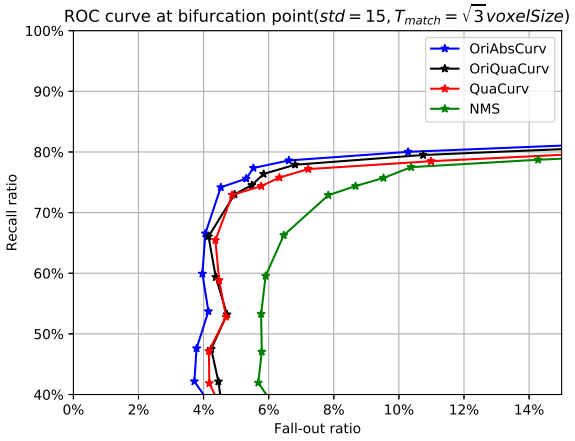

Figure 12. Detection of bifurcation points (only).

4. Evaluation

4.1. Synthetic vessel volume

We used our modification[3] of a method generating synthetic 3D vessel tree data [13] that includes CT-like volume and ground truth vessel centerline tree, *e.g.* Fig. 10. We generate 15 artificial volumes $100 \times 100 \times 100$ containing synthetic vascular trees with voxel intensities in the range 0 to 512. The size of each voxel is 0.046 mm. We use additive Gaussian noise [16] with *std* 15.

Evaluation setup. Our evaluation system follows [18]. We first apply the Frangi filter [11] with hyperparameters $\alpha = 0.5$, $\beta = 0.5$, $\gamma = 30$, $\sigma_{min} = 0.023$ mm and $\sigma_{max} = 0.1152$ mm. The filter computes a *tubularness measure* and estimates tangent l_p at each voxel p. Then we threshold the tubularness measure to remove background pixels. Then we use non-maximum suppression[4] (NMS) resulting in voxel set Ω. We use a 26-connected neighborhood system N. Next, we optimize our new join energy (10) to disambiguate tangent orientation and estimate centerline location, see Sec. 3.2. The hyperparameters are $\gamma = 3.80$ (see energy (5)), $\lambda = 18.06$ (see energy (10)), $\tau = \cos 70°$ (see equation (6)), and the maximum number of iterations is 1500 for both TRWS and Levenberg-Marquardt. Finally, we extract oriented vessel tree centerline as the minimum spanning tree of the complete graph.

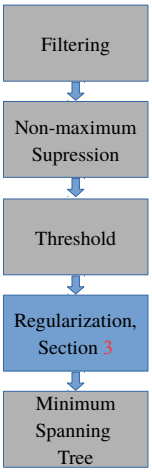

Energy (10) assumes a quadratic curvature term (3). However, if we replace it with (1) we get an absolute curva-

[3] https://gitlab.com/echesakov/VascuSynth

[4] The use of NMS is mainly for data reduction. Our method is able to work on thresholded data directly, see Fig. 3(d).

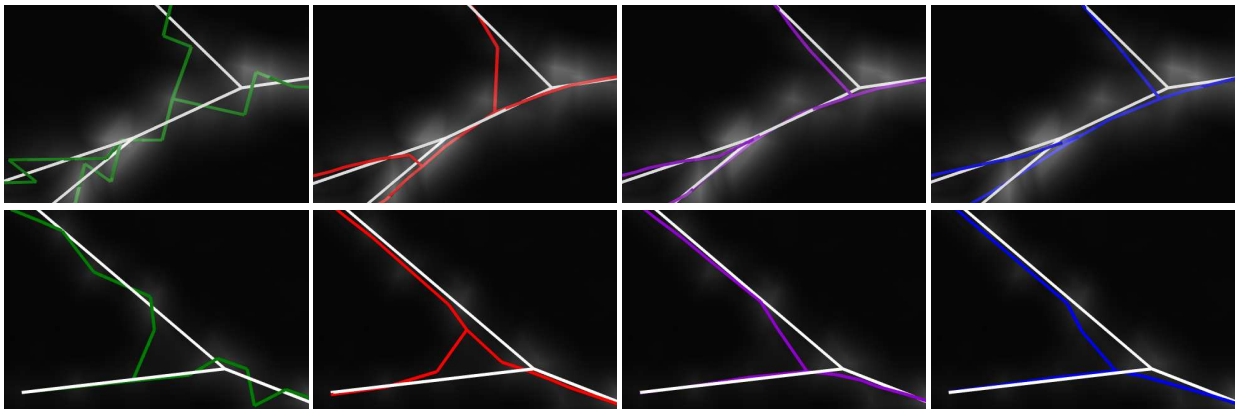

(a) (b) (c) (d)

Figure 13. Examples of the results around bifurcations. White line is the ground truth tree. A tree extracted from NMS ouput directly (without regularization) is shown in (a). Solution of (4) [18] is (b). Our model (10) is (c). Our model (10) with absolute curvature is (d).

ture variant of our energy.

We evaluate different regularization methods including energy (4) (QuaCurv), energy (10) with either quadratic curvature (OriQuaCurv) or absolute curvature (OriAbsCurv) within the system outline above. We also compare to a tracing method [3] and medial axis [4].

We adopt *receiver operating characteristic* (ROC) curve methodology for evaluation of our methods and [4]. We compute *recall* and *fall-out* statistics of an extracted vessel tree for different levels of the threshold. The computed statistics define the ROC curve.

While ground truth is defined by locations at bifurcations and leaves of the tree, all evaluated methods yield densly sampled points on the tree. Therefore, we resample both ground truth and reconstructed tree with step size 0.0023 mm. For each point on one tree, we find the nearest point on the other tree and compute the Euclidean distance. If the distance is less than $\max(r, c)$ voxels, this pair of points is considered a *match*. Here r is the vessel radius at the corresponding point of the ground truth and $c = 0.7$ is a matching threshold measured in voxels. The recall is

$$\frac{N_{GTmatch}}{N_{GTtotal}}$$

where $N_{GTmatch}$ is the number of matched points in the ground truth and $N_{GTtotal}$ is the total number of points in the ground truth. The fall-out is

$$1 - \frac{N_{RTmatch}}{N_{RTtotal}}$$

where $N_{RTmatch}$ is the number of matched points in the reconstructed tree and $N_{RTtotal}$ is the total number of points in the reconstructed tree.

The tracing method of [3] requires a seed points list as an input. We generate four seed lists as described in Fig. 11. The ROC curves in Fig. 11 favour our method. Since bifurcations is only a fraction of the data, the improvements around bifurcations are largely unnoticed in these curves. Therefore, we compute the ROC curves for only bifurcation nodes. We use a bigger matching threshold $c = \sqrt{3}$ voxels. The results are shown in Fig. 12 where the gap between methods is bigger. Also we compute angle errors at bifurcations, see Fig. 14. A few representative examples are in Fig. 13.

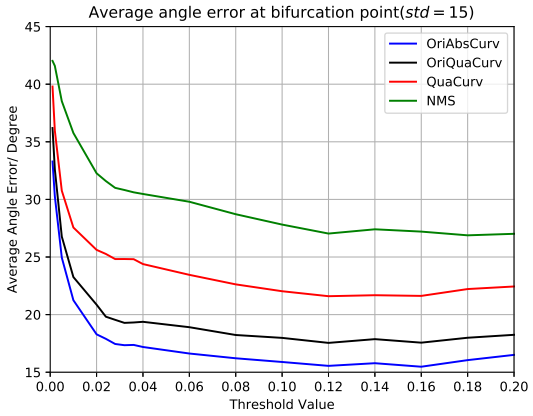

Figure 14. Bifurcaton angle errors (at detected bifurcations).

4.2. Real vessel data

We obtained our qualitative experimental results using a real micro-CT scan of mouse's heart as shown in Fig.15. The size of the volume is $585 \times 525 \times 892$ voxels. Most of the vessels are thinner than the voxel size. Due to the size of the volume, the problem has higher computational cost than in Sec. 4.1. We built custom GPU implementation of Levenberg-Marquardt algorithm to handle the large volume size [7]. Figure 16 shows the reconstructed centerline. Figure 17 demonstrate a significant improvement of centerline estimation around bifurcations.

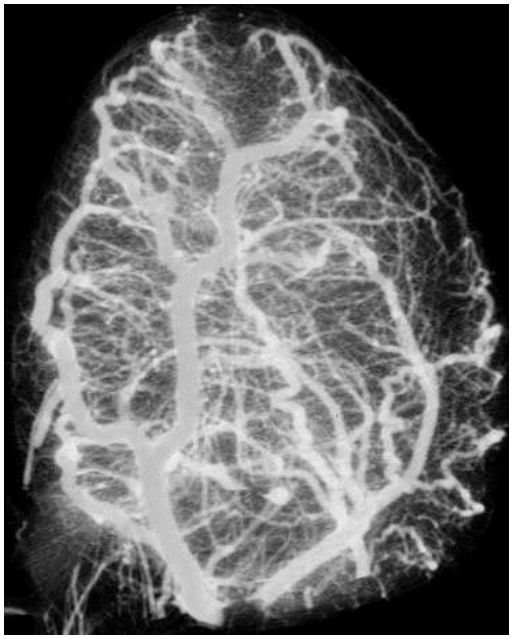

(a) cardiac microscopy CT volume

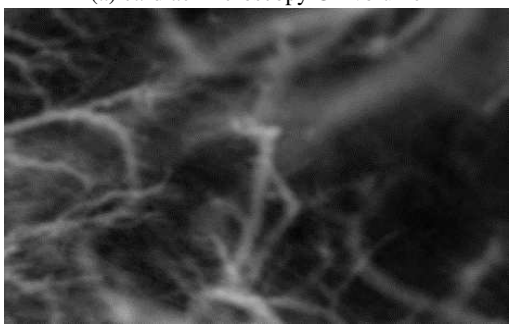

(b) zoom-in

Figure 15. Visualization (MIP) of the raw volumetric data obtained from a mouse heart by *microscopic computer tomography*.

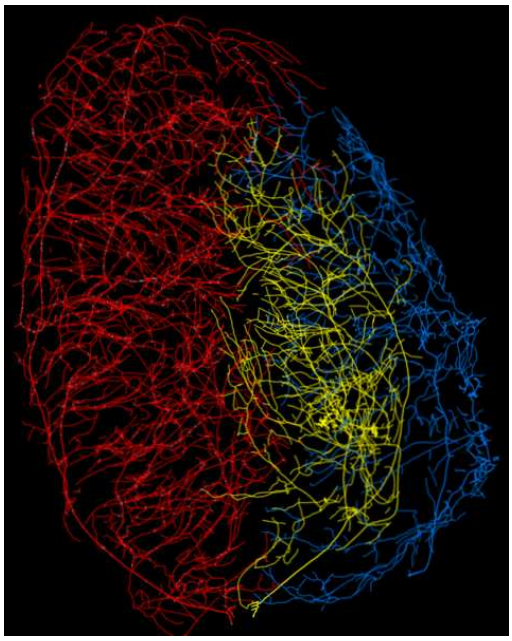

Figure 16. Vessel tree reconstruction from real data in Fig. 15 based on our method for estimating centerline tangents using prior knowlegde about vessel divergence. The final tree structure is extracted by MST on K-nearest-neighbour (KNN) weighted graph with edge weights w_{pq} defined as the average *arc-length* between neighbors p and q for two circles containing p and q and tangential to either l_p or l_q. Different colors denote three main branches.

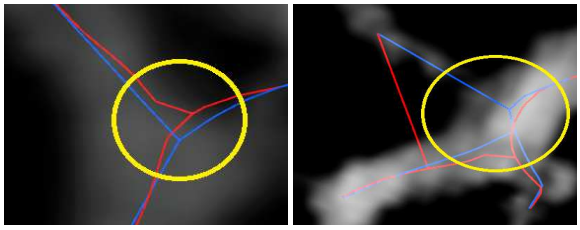

Figure 17. Representative results on **real data**. Red shows the result of [18], see (4). Blue shows the centerline produced by our directed vessel estimation model (10) including the divergence prior and absolute curvature regularization. We highlight improvements at bifurcations due to better estimation of vessel orientations. As shown, mistakes lead to wrong connectivity (tubular) graphs. The real data results are consistent with the synthetic ones in Fig.13.

5. Conclusions and Future work

We propose divergence prior for a vector field reconstruction problem. In the contest of vessel tree estimation, we use the divergent vessel prior to estimate vessel directions disambiguating orientations produced by the Frangi filter. Our method significnatly improves the accuracy of reconstruction at bifurcations, reducing the corresponding angle estimation errors by about 50%.

There are interesting extentions for our work on estimating vessel orientations. For example, such orientations can be directly used for extracting vessel tree topology or connectivity. Instead of using standard MST on undirected graphs, *e.g.* as in [18], we can now use Chu-Liu-Edmonds algorithm [8, 9] to compute a minimum spanning *arborescence* (a.k.a. directed rooted tree) on a directed weighted graph where a weight of any edge (p, q) estimates the length of a possible direct "vessel" connection specifically from p to q. Such a weight can estimate the *arc length* from p to q along a unique circle such that it contains p and q. This circle is coplanar with l_p and q, and is tangential to l_p. However, such a constant curvature path from p to q works as a good estimate for a plausible vessel connection from p to q only if $\langle l_p, pq\rangle > 0$; otherwise there should be no edge from p to q. This implies a directed graph since edges (p, q) and (q, p) will be determined by two different tangents l_p or l_q and two different conditions $\langle l_p, pq\rangle > 0$ or $\langle l_q, qp\rangle > 0$.

Finally, it is possible to explore optimal subtree algorithms [30, 31] as more advanced alternatives to MST or arborescence technqiues.

References

[1] T. D. Alter and R. Basri. Extracting salient curves from images: An analysis of the saliency network. *IJCV*, 27(1):51–69, 1998. 2

[2] L. Alvarez, P.-L. Lions, and J.-M. Morel. Image selective smoothing and edge detection by nonlinear diffusion. ii. *SIAM Journal on numerical analysis*, 29(3):845–866, 1992. 2

[3] S. R. Aylward and E. Bullitt. Initialization, noise, singularities, and scale in height ridge traversal for tubular object centerline extraction. *IEEE transactions on medical imaging*, 21(2):61–75, 2002. 2, 6, 7

[4] S. Bouix, K. Siddiqi, and A. Tannenbaum. Flux driven automatic centerline extraction. *Medical image analysis*, 9(3):209–221, 2005. 6, 7

[5] K. Bredies, T. Pock, and B. Wirth. Convex relaxation of a class of vertex penalizing functionals. *Journal of Mathematical Imaging and Vision*, 47(3):278–302, 2013. 2

[6] T. F. Chan and J. Shen. Nontexture inpainting by curvature-driven diffusions. *Journal of Visual Communication and Image Representation*, 12(4):436–449, 2001. 2

[7] E. Chesakov. Vascular tree structure: Fast curvature regularization and validation. *Electronic Thesis and Dissertation Repository. The University of Western Ontario*, (3396), 2015. Master of Science thesis. 7

[8] Y. J. Chu and T. H. Liu. On the shortest arborescence of a directed graph. *Science Sinica*, 14:1396–1400, 1965. 8

[9] J. Edmonds. Optimum branchings. *J. Res. Nat. Bur. Standards*, 71B(4), October- December 1967. 8

[10] A. Enquobahrie, L. Ibanez, E. Bullitt, and S. Aylward. Vessel enhancing diffusion filter. *The Insight Journal*, 1:1–14, 2007. 1

[11] A. F. Frangi, W. J. Niessen, K. L. Vincken, and M. A. Viergever. Multiscale vessel enhancement filtering. In *MICCAI'98*, pages 130–137. Springer, 1998. 1, 3, 4, 5, 6

[12] G. Guy and G. Medioni. Inferring global perceptual contours from local features. In *CVPR*, 1993. 2

[13] G. Hamarneh and P. Jassi. Vascusynth: simulating vascular trees for generating volumetric image data with ground-truth segmentation and tree analysis. *Computerized medical imaging and graphics*, 34(8):605–616, 2010. 6

[14] S. Heber, R. Ranftl, and T. Pock. Approximate envelope minimization for curvature regularity. In *ECCV*, 2012. 1, 2

[15] V. Kolmogorov. Convergent tree-reweighted message passing for energy minimization. *PAMI*, 28(10):1568–1583, 2006. 3, 5

[16] G. Lehmann. Noise simulation. *The Insight Journal*, January-June 2010. 6

[17] G. Li and S. W. Zucker. Differential geometric inference in surface stereo. *PAMI*, 32(1):72–86, 2010. 2

[18] D. Marin, Y. Zhong, M. Drangova, and Y. Boykov. Thin structure estimation with curvature regularization. In *International Conference on Computer Vision (ICCV)*, Santiago, Chile, December 2015. 1, 2, 3, 5, 6, 7, 8

[19] S. Moccia, E. De Momi, S. El Hadji, and L. Mattos. Blood vessel segmentation algorithms — review of methods, datasets and evaluation metrics. *Computer Methods and Programs in Biomedicine*, 158:71–91, 2018. 1

[20] P. MomayyezSiahkal and K. Siddiqi. 3d stochastic completion fields for mapping connectivity in diffusion mri. *PAMI*, 35(4):983–995, 2013. 2

[21] C. Nieuwenhuis, E. Toeppe, L. Gorelick, O. Veksler, and Y. Boykov. Efficient squared curvature. In *CVPR*, Columbus, Ohio, 2014. 1, 2

[22] C. Olsson and Y. Boykov. Curvature-based regularization for surface approximation. In *Conference on Computer Vision and Pattern Recognition (CVPR)*, pages 1576–1583. IEEE, 2012. 2, 3

[23] C. Olsson, J. Ulén, and Y. Boykov. In defense of 3d-label stereo. In *CVPR*, pages 1730–1737. IEEE, 2013. 2

[24] C. Olsson, J. Ulén, Y. Boykov, and V. Kolmogorov. Partial enumeration and curvature regularization. In *ICCV*, pages 2936–2943. IEEE, 2013. 1, 2, 3

[25] T. Schoenemann, F. Kahl, and D. Cremers. Curvature regularity for region-based image segmentation and inpainting: A linear programming relaxation. In *ICCV*, Kyoto, 2009. 1, 2

[26] T. Schoenemann, F. Kahl, S. Masnou, and D. Cremers. A linear framework for region-based image segmentation and inpainting involving curvature penalization. *IJCV*, 2012. 2

[27] K. Siddiqi and S. Pizer. *Medial representations: mathematics, algorithms and applications*, volume 37. Springer Science & Business Media, 2008. 1

[28] P. Strandmark and F. Kahl. Curvature regularization for curves and surfaces in a global optimization framework. In *EMMCVPR*, pages 205–218. Springer, 2011. 1, 2

[29] M. Tang, F. Perazzi, A. Djelouah, I. B. Ayed, C. Schroers, and Y. Boykov. On regularized losses for weakly-supervised cnn segmentation. In *European Conference on Computer Vision (ECCV)*, Munich, Germany, September 2018. 1

[30] E. Turetken, F. Benmansour, B. Andres, P. Glowacki, H. Pfister, and P. Fua. Reconstructing curvilinear networks using path classifiers and integer programming. *IEEE Transactions on Pattern Analysis and Machine Intelligence (TPAMI)*, 38(12):2515–2530, December 2016. 1, 2, 8

[31] E. Turetken, G. Gonzalez, C. Blum, and P. Fua. Automated reconstruction of dendritic and axonal trees by global optimization with geometric priors. *Neuroinformatics*, 9(2-3):279–302, 2011. 1, 2, 8

[32] L. R. Williams and D. W. Jacobs. Stochastic completion fields: A neural model of illusory contour shape and salience. *Neural Computation*, 9(4):837–858, 1997. 2

[33] O. Woodford, P. Torr, I. Reid, and A. Fitzgibbon. Global stereo reconstruction under second-order smoothness priors. *PAMI*, 31(12):2115–2128, 2009. 2

[34] S. Wright and J. N. Holt. An inexact levenberg-marquardt method for large sparse nonlinear least squres. *The Journal of the Australian Mathematical Society. Series B. Applied Mathematics*, 26(04):387–403, 1985. 5